Journal of Materials Chemistry A

ROYAL SOCIETY OF CHEMISTRY

PAPER

View Article Online
View Journal

Check for updates

Cite this: DOI: 10.1039/d6ta02103d

Amorphous iron vanadate positive electrode enabling fast pseudocapacitive sodium-ion storage

Xiaoqing Chang,† Dafu Tang,† Sicheng Fan, Guiyang Gao and Qiulong Wei *

Amorphous iron vanadate (a-FVO) is a promising positive electrode for sodium-ion hybrid capacitors owing to its high-rate capability and abundant raw material. However, the correlation between elemental composition of a-FVO and its electrochemical properties remains poorly understood. Herein, we investigate the electrochemical performance of a-FVO with various Fe/V ratios for sodium-ion storage. It is found that a decrease in the Fe/V ratio enhances the reversible capacity of the electrode, while increasing the charge-transfer energy barrier and hindering Na^+ diffusion. *Ex situ* structural characterization reveals that the increased V content strengthens the interactions between metal–oxygen bonds and Na^+ ions. Importantly, a-FVO with an Fe/V molar ratio of 1 : 2 features an optimal configuration of active sites and bridging bonds, achieving balanced specific capacity and rate capability along with good cycling stability. Kinetic analysis reveals a pseudocapacitive-dominated process (capacitive contribution of ~90%) of Na^+ storage in it, accompanied by reversible local bond vibrations. This work provides insights into the important role of the local bonding environments in pseudocapacitive charge storage, which is promising for high-rate electrochemical capacitors.

Received 11th March 2026
Accepted 27th May 2026

DOI: 10.1039/d6ta02103d

rsc.li/materials-a

1 Introduction

With the growing market demand for intelligent electric-driven devices, there is a critical need for electrochemical energy storage (EES) devices capable of rapid high-energy delivery.[1–3] Current mainstream EES devices, such as high-energy secondary batteries and high-power supercapacitors, exhibit an inherent trade-off between energy density and power density.[4] Sodium-ion hybrid capacitors (SIHCs) consist of battery-type and capacitor-type electrodes, thus enabling simultaneous high energy and power density.[5–7] They hold great promise for widespread application in large-scale, high-power energy storage scenarios such as smart grids, electric vehicles, and data centers.[8] Recently, progress has been made in the development of high-rate negative electrode materials such as titanium oxides,[9,10] bismuth-based alloys,[11,12] and solvent-co-intercalated graphite.[13] Although the widely employed porous carbon positive electrodes (*e.g.*, activated carbon) deliver excellent rate performance and ultra-long cycle life based on electric double-layer capacitive reactions, they suffer from low specific capacity and variations in electrolyte concentration during operation.[14] In addition, the carbon positive electrodes with low compaction density require thick electrodes when matched with high-capacity negative electrodes,[15] which compromises the power density and volumetric energy density of the SIHCs.[16] Therefore, developing high-capacity positive electrode materials with fast charge storage kinetics is crucial to alleviate the capacity mismatch between positive and negative electrodes and satisfy the requirements of next-generation high-performance SIHCs.

Pseudocapacitive materials store charge *via* Faradaic redox reactions while exhibiting capacitor-like kinetics.[17] They deliver high specific capacity at high rates, which concurrently achieves high energy and power density.[18] Compared with crystalline materials, amorphous materials with long-range disorder avoid lattice constraints and facilitate pseudocapacitive charge storage.[19] It was reported that the amorphous $Na_3V_2(PO_4)_3$ prepared by a wet-chemical route stores/releases Na^+ ions through the pseudocapacitive-dominant reaction rather than the intercalation reaction of crystalline $Na_3V_2(PO_4)_3$,[20] as evidenced by sloping charge–discharge curves without a plateau at ~3.4 V *vs.* Na^+/Na. When crystalline $Na_2VO(SO_4)_2$ is transformed into an amorphous state *via* ball milling, its specific capacity (from 62.3 to 83.4 mAh g^{-1} at 0.01 A g^{-1}) and rate performance are significantly improved with an increased capacitive contribution (from 70% to 82% at 0.6 mV s^{-1}),[21] demonstrating the great potential of amorphization in optimizing reaction kinetics. Therefore, amorphous materials with abundant active sites and open ion diffusion channels facilitate the rapid insertion/extraction of large amounts of Na^+ ions, making them highly promising pseudocapacitive materials.

Iron vanadate (FeV_xO_y) is a promising positive electrode candidate for sodium-ion storage due to its high reactivity

State Key Laboratory of Physical Chemistry of Solid Surfaces, Fujian Key Laboratory of Surface and Interface Engineering for High Performance Materials, College of Materials, Xiamen University, Xiamen 361005, China. E-mail: qlwei@xmu.edu.cn

† These authors contributed equally to this work.

toward multiple redox couples and abundant iron reserves.[22,23] Compared with widely used activated carbon, FeV_xO_y exhibits higher specific capacity and compaction density, allowing for better space utilization within devices.[13] It was reported that amorphous $FeVO_4$ electrodes experience a pseudocapacitive-dominated Na^+ insertion and extraction, as verified by electrochemical kinetic analysis.[24] They display a quasi-rectangular cyclic voltammetry (CV) curve with no distinct redox peaks and deliver a reversible specific capacity of ~100 mAh g^{-1}, surpassing that of the crystalline counterpart (~30 mAh g^{-1}). As a typical bimetallic oxide, the stoichiometric ratio of the two transition metals in FeV_xO_y may determine the density of active sites, the local atomic bonding configurations, and electronic states, thereby modulating reversible capacity and sodium-ion transport rates.[25] However, existing research on FeV_xO_y electrodes primarily focuses on the use of specific stoichiometric compounds (such as $FeVO_4$ (ref. 24) and Fe_2VO_4 (ref. 26)), whereas the correlation between the Fe/V ratio and electrochemical properties, as well as structural evolution during cycling remain unexplored.

In this work, we investigate the differences in electrochemical properties of amorphous iron vanadate (a-FVO) across varying Fe/V ratios for sodium-ion storage. Variations in the Fe/V ratio modulate the metal–oxygen bonding configurations and the valence states of cations, as demonstrated by Raman spectroscopy and X-ray photoelectron spectroscopy (XPS). With a decreased Fe/V ratio, the enhanced specific capacity of a-FVO stems from the increased V content. Charge storage kinetics elucidated by impedance spectroscopy, capacitive contribution and ion diffusivity analysis reveal that the Fe–O–V bridging bonds play a vital role in determining the rate capability of a-FVO. Structural evolution analysis based on *ex situ* X-ray diffraction (XRD) and Raman spectroscopy indicates that Fe–O–V bridging bonds stabilize the local structure, and that the structural evolution of a-FVO electrodes is composition-independent, without obvious phase transitions during electrochemical cycling. Importantly, a-FVO with an Fe/V ratio of 1 : 2 achieves an optimal balance between specific capacity and rate performance, making it a promising pseudocapacitive positive electrode for sodium-ion storage.

2 Results and discussion

2.1 Structural and morphological characterization

a-FVO particles with different Fe/V stoichiometric ratios were synthesized by a simple solvothermal method using the mixed iron and vanadium source in proportion.[26] It was reported that Fe in the $FeV_3O_{8.7}\cdot nH_2O$ positive electrodes shows low redox activity and primarily serves as a bridge.[27] Therefore, increasing the V content in a-FVO is expected to increase the reaction sites. To verify this hypothesis, a series of a-FVO samples with decreasing Fe/V ratios (Fe/V = 1 : 1, 1 : 2, 1 : 4, denoted as F1V1O, F1V2O, and F1V4O, respectively) were prepared. Inductively coupled plasma optical emission spectroscopy (ICP-OES) results confirm that the measured values of the Fe/V atomic ratios are consistent with the designed values across the compositional series (Fig. 1a). XRD patterns of the three samples present featureless diffraction profiles without distinct peaks (Fig. 1a), indicating their amorphous nature. Raman spectroscopy was carried out to characterize the local bonding

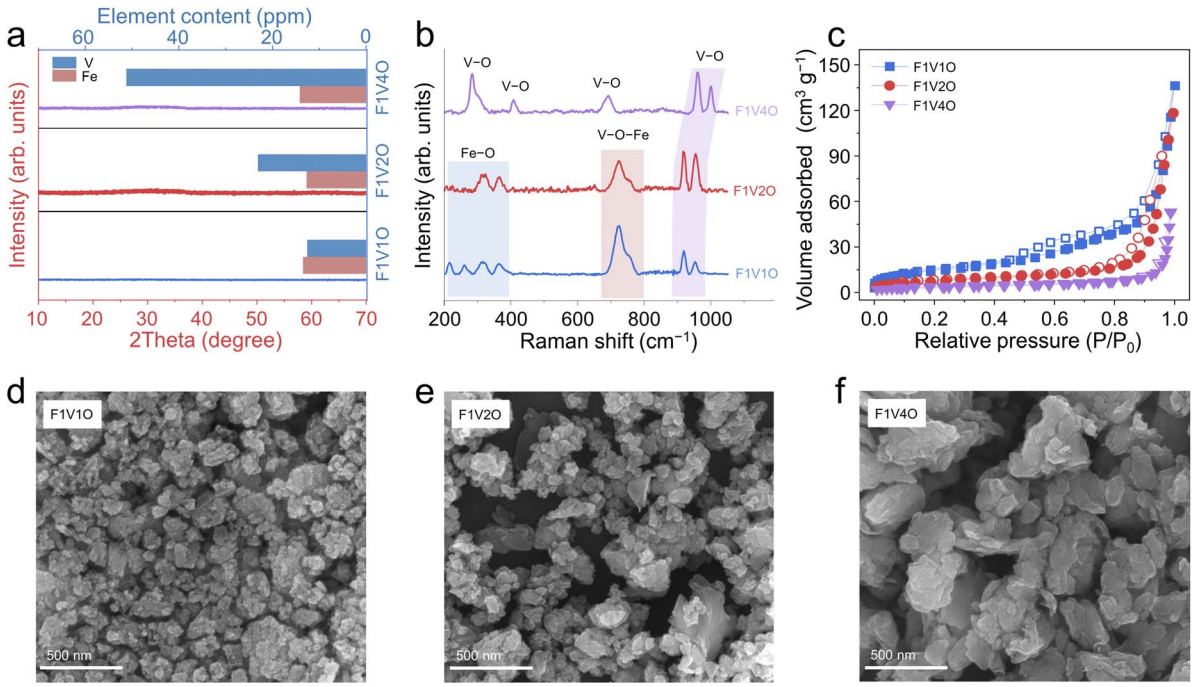

Fig. 1 (a) XRD patterns and ICP-OES measurement results, (b) Raman spectra, and (c) N_2 adsorption–desorption isotherms of a-FVO powders. SEM images of (d) F1V1O, (e) F1V2O, and (f) F1V4O.

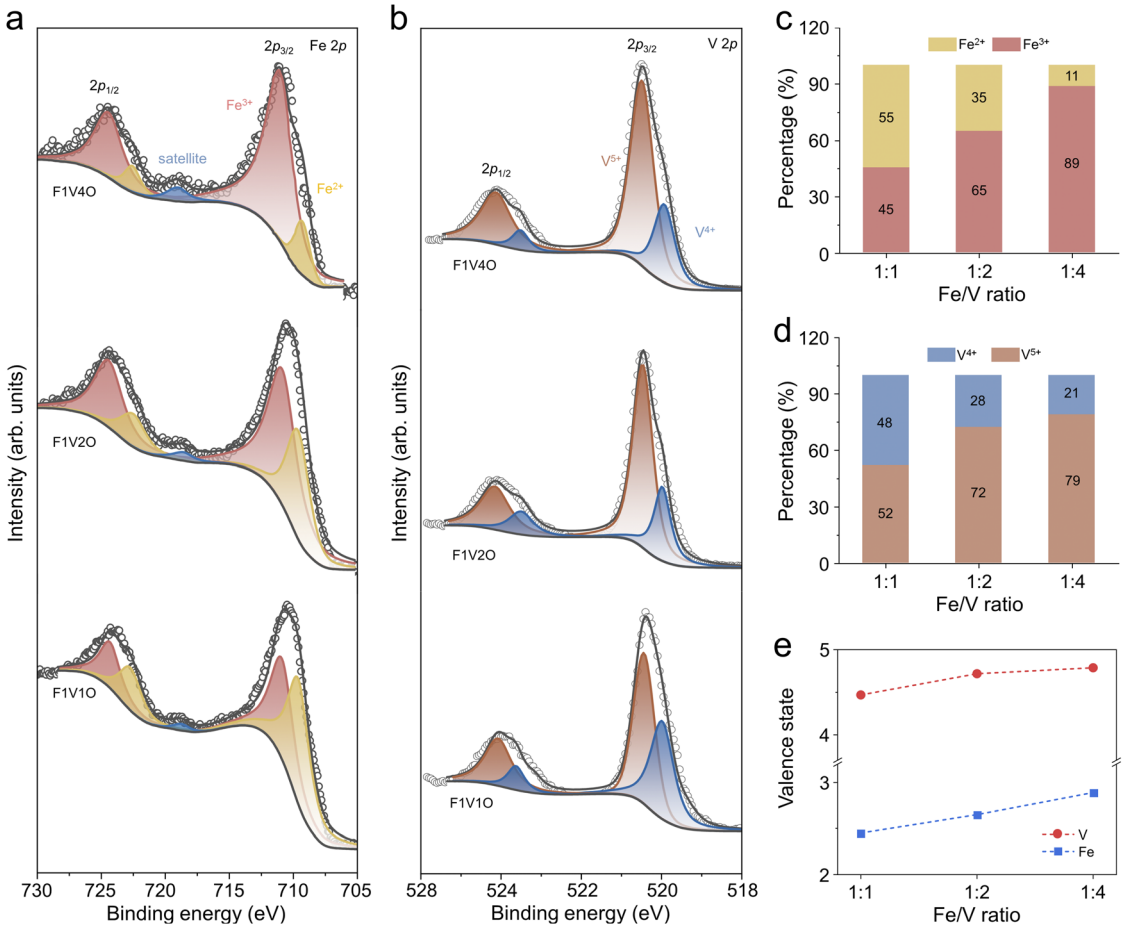

Fig. 2 (a) Fe 2p and (b) V 2p XPS spectra of the a-FVO powders. (c) Quantitative ratio of Fe^{2+} and Fe^{3+} in a-FVO calculated from (a). (d) Quantitative ratio of V^{4+} and V^{5+} in a-FVO calculated from (b). (e) Average valence state of Fe and V in a-FVO with various Fe/V ratios.

environment of a-FVO. The Raman signals of the characteristic vibrational modes for the three samples are mainly located at 200–400, 700–800, and 850–1000 cm^{-1} (Fig. 1b). Signals located in the lower Raman shift region mainly correspond to Fe–O stretching vibrations, where the peak at ~220 cm^{-1} is assigned to A_{1g} modes and peaks at ~280 and ~400 cm^{-1} belong to E_g modes.[28,29] The broad peak at ~723 cm^{-1} corresponds to Fe–O–V bridging bonds,[24,30] and the splitting peaks observed between 800 and 1000 cm^{-1} originate from V–O stretching vibrations.[31,32] F1V2O and F1V4O show stronger V–O peaks compared to F1V1O, indicating that the decrease in the Fe/V ratio induces more V–O bonds. Nitrogen adsorption–desorption measurements (Fig. 1c) reveal a positive correlation between the Fe/V ratio and specific surface area (52.6 $m^2\ g^{-1}$ for F1V1O, 26.4 $m^2\ g^{-1}$ for F1V2O, and 11.0 $m^2\ g^{-1}$ for F1V4O). The scanning electron microscopy (SEM) images (Fig. 1d–f) show that the three samples consist of irregular particles. Their particle sizes increase with the decline of the Fe/V ratio (~50 nm for F1V1O, ~85 nm for F1V2O, and ~200 nm for F1V4O), which is consistent with the specific surface area results (Fig. 1c). Energy Dispersive Spectroscopy (EDS) mappings indicate the existence of Fe, V and O in the three a-FVO samples and the uniform distribution of elements in all samples (Fig. S1).

2.2 Valence state characterization of transition metals

XPS was conducted to investigate the valence states of transition metals in the samples. The Fe $2p_{3/2}$ binding energy of 709.6 eV is assigned to Fe^{2+} (Fe–O–V bond),[33] while the peak at 710.8 eV corresponds to Fe^{3+} (Fe–O) (Fig. 2a).[34] For the V $2p_{3/2}$ spectra (Fig. 2b), the binding energy of 515.9 eV is consistent with V^{4+} (Fe–O–V bond), while the peak located at 517.2 eV is assigned to V^{5+} (V–O bond).[35] The quantitative deconvolution results of Fe 2p spectra show that the proportion of Fe^{3+} increases from 45% to 65% and further to 89%, whereas the proportion of Fe^{2+} decreases from 55% to 35% and further to 11% (Fig. 2c). These results indicate that the decreased Fe/V ratio reduces the content of Fe–O–V bridging bonds. Quantitative analysis of the V 2p spectra indicates a similar increase in the proportion of V^{5+} along with a decrease in the proportion of V^{4+} (Fig. 2d), suggesting an increase in the content of V–O bonds. EDS elemental mappings (Fig. S1) confirm uniform distribution of Fe and V throughout the particles, indicating that the bulk and surface regions of the a-FVO samples have the same Fe^{2+}/Fe^{3+} and V^{4+}/V^{5+} ratios. Fig. 2e shows the average chemical valences of Fe and V in the three samples calculated based on the deconvolution results. With the decreasing Fe/V ratio, the average chemical valence of Fe increases from +2.45 to +2.65

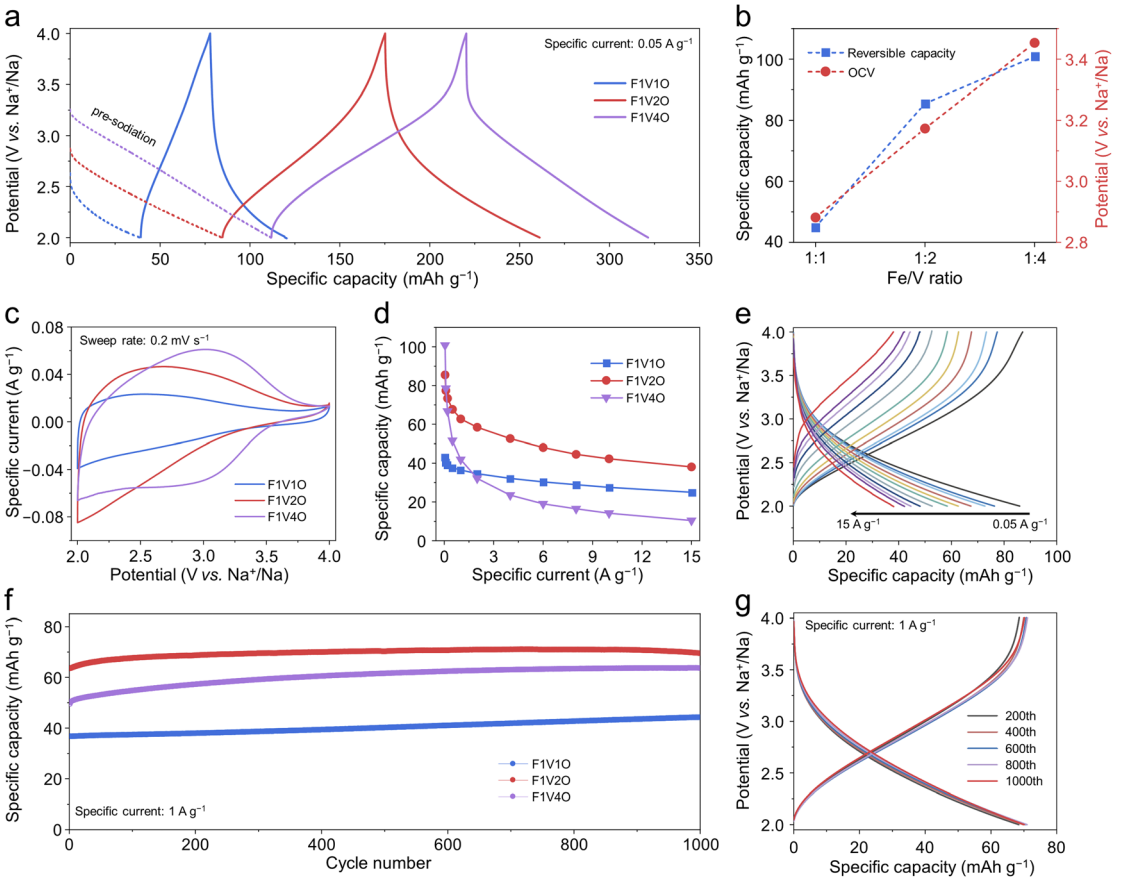

Fig. 3 (a) GCD profiles of the three a-FVO electrodes at 0.05 A g^{-1}. (b) Reversible capacity and OCV of the a-FVO electrodes with various Fe/V ratios. (c) CV curves at 0.2 mV s^{-1}. (d) Rate performance. (e) GCD profiles of F1V2O at various specific currents. (f) Cycling performance at 1 A g^{-1}. (g) GCD profiles of F1V2O during cycling at 1 A g^{-1}.

and further to +2.89, and that of V also increases from +4.47 to +4.72 and further to +4.79. The elevated V valence strengthens the polarization effect on O atoms and weakens the electron-donating capability of O in the Fe–O–V bond, thereby weakening the shielding effect on Fe and raising its valence state.[36,37] These results demonstrate that regulating the Fe/V ratio modulates the local bonding structure, thereby influencing the valence states of the transition metals in a-FVO.

2.3 Electrochemical performance

The electrochemical behavior of a-FVO was measured in coin cells employing sodium metal as a counter/reference electrode and 1 M $NaPF_6$ in diglyme as the electrolyte. Fig. 3a shows the galvanostatic charge–discharge (GCD) profiles of the three a-FVO electrodes at a specific current of 0.05 A g^{-1} in the potential range of 2.0–4.0 V *vs.* Na^+/Na. The open-circuit voltage (OCV) of the a-FVO electrodes increases with a declining Fe/V ratio (2.68 V for F1V1O, 3.17 V for F1V2O, and 3.41 V for F1V4O), which is attributed to the change in the oxidation states of the transition metals.[38,39] Because the as-synthesized a-FVO samples are inherently sodium-deficient, the electrodes require electrochemical pre-sodiation prior to charge–discharge cycling. The initial sodiation capacity of F1V2O lies between those of the other two compositions, which is consistent with its intermediate transition-metal valence state. The desodiation and sodiation profiles of all three electrodes show sloping curves, indicating a capacitor-like behavior without phase transitions during the insertion/extraction of Na^+ ions. The initial Coulombic efficiency of F1V1O, F1V2O and F1V4O is 109.9%, 95.0% and 93.3%, respectively (Table S1). The reversible specific capacities of F1V1O, F1V2O and F1V4O are 45.0, 85.5 and 100.8 mAh g^{-1} at 0.05 A g^{-1} (Fig. 3b) respectively, demonstrating a dependence of reversible capacity on the Fe/V ratio. Although the specific surface area of a-FVO positive electrodes decreases with the decreased Fe/V ratio, their specific capacity increases, indicating that their capacity is not determined by morphological effects. The d-band center of V^{4+} is closer to the Fermi level with a lower oxidation energy barrier, while Fe^{2+} requires a stronger electric field driving force and shows weak electrochemical activity;[27] thus Na^+ ions preferentially undergo storage reactions at V sites.[40,41] The variation of the Fe/V ratio regulates the proportion of active sites and available Na^+ storage sites. Although elevated vanadium content improves specific capacity, abundant intrinsic defects reduce the initial Coulombic efficiency and reversibility of sodium ion insertion/extraction. The quasi-rectangular CV curves of the cycled F1V2O

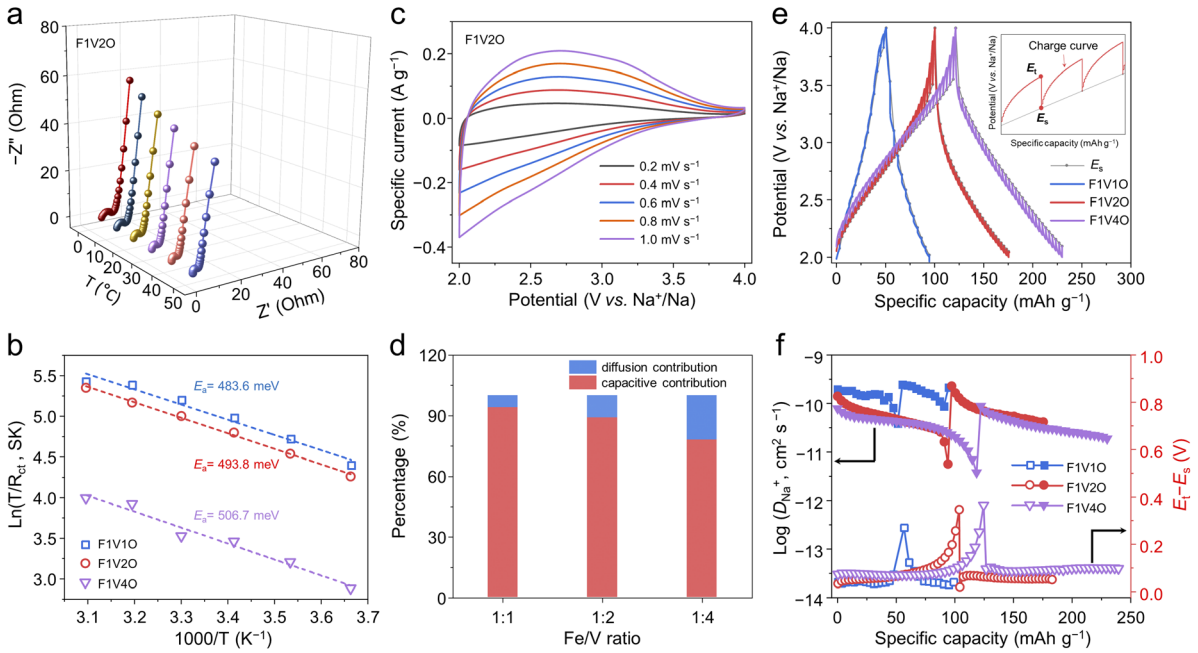

Fig. 4 (a) Nyquist plots of the F1V2O electrode at various temperatures. (b) Arrhenius plots of the a-FVO electrodes. (c) CV curves of F1V2O at sweep rates of 0.2–1.0 mV s^{-1}. (d) Capacitive and diffusion contributions for the a-FVO electrodes at 1 mV s^{-1}. (e) GITT curves of the three a-FVO electrodes. The inset is a local magnification of the relaxation curve for F1V2O. (f) Logarithm D_{Na^+} and E_t–E_s *vs.* specific capacity plots of the a-FVO electrodes.

electrode further confirm the capacitive-dominant Na^+ insertion/extraction behavior (Fig. 3c).

The rate performance of the a-FVO electrodes for electrochemical Na^+ insertion/extraction is shown in Fig. 3d. F1V1O exhibits high capacity retention at high rates, but delivers limited capacity. Conversely, F1V4O delivers a higher capacity but undergoes severe capacity decay at higher rates. F1V2O with a modest Fe/V ratio achieves a favorable balance between specific capacity and rate performance, retaining a capacity of 85.5, 52.6 and 38.2 mAh g^{-1} at the specific current of 0.05, 4 and 15 A g^{-1}, respectively. It also maintains sloping GCD profiles and low polarization with increasing charge–discharge rates (Fig. 3e). Compared with the reported pseudocapacitive positive electrode (Table S2), the amorphous F1V2O positive electrode exhibits superior rate capability but a lower reversible capacity. In addition, in contrast to amorphous F1V2O, crystalline F1V2O shows a low specific capacity of 30 mAh g^{-1} and exhibits broad redox peaks in its CV curve (Fig. S2), revealing that amorphous FVO positive electrodes have a stronger Na^+ storage capability than their crystalline counterparts.

When cycled at a low specific current of 0.2 A g^{-1} (Fig. S3), F1V2O delivers a reversible capacity of 78.94 mAh g^{-1} lying between those of F1V1O and F1V4O, with 95% capacity retention after 100 cycles. All three electrodes show excellent long-term cycling stability (105% capacity retention after 1000 cycles for F1V2O) at 1 A g^{-1} (Fig. 3f). The GCD curves of F1V2O during cycling overlap well with a slight capacity increase (Fig. 3g), which may be attributed to the gradual activation of internal transition metals within the material. Furthermore, *ex situ* XRD patterns of the three a-FVO electrodes after 1000 cycles still lack distinct diffraction peaks, confirming preservation of the amorphous structure after long-term cycling (Fig. S4). The above electrochemical results indicate that a Fe/V ratio of 1 : 2 in a-FVO optimizes Na^+ insertion/extraction, achieving an optimal balance among high capacity, high-rate capability and long-term cycle stability.

2.4 Kinetic analysis of charge storage

Electrochemical impedance spectroscopy (EIS) measurements were performed to investigate the reaction kinetics of a-FVO electrodes with different Fe/V ratios. Fig. 4a, S5a and b show the EIS spectra of the three a-FVO electrodes after full desodiation at various temperatures (0–50 °C). Their Nyquist plots all exhibit a semicircle in the high-frequency region and a straight line in the low-frequency region, corresponding to charge-transfer resistance (R_{ct}) and Warburg impedance based on the equivalent circuit given in Fig. S5a and b. The R_{ct} values of the three electrodes remain relatively low (2–4 Ω) and decline with increasing temperature (Fig. S5c). The charge-transfer activation energy could be calculated by fitting the $\ln(T/R_{ct})$ *vs.* $1000/T$ plots based on the Arrhenius equation (eqn (1)):[42,43]

$$\sigma T = A\exp\left(\frac{E_a}{k_B T}\right) \quad (1)$$

where A is the pre-exponential factor, E_a is the apparent activation energy, k_B is the Boltzmann constant, σ is the ionic conductivity, and T is the absolute temperature. The apparent activation energy for charge transfer of F1V1O (483.6 meV) is lower than those of F1V2O (493.8 meV) and F1V4O (506.7 meV) (Fig. 4b). This means that a-FVO with a higher Fe/V ratio could

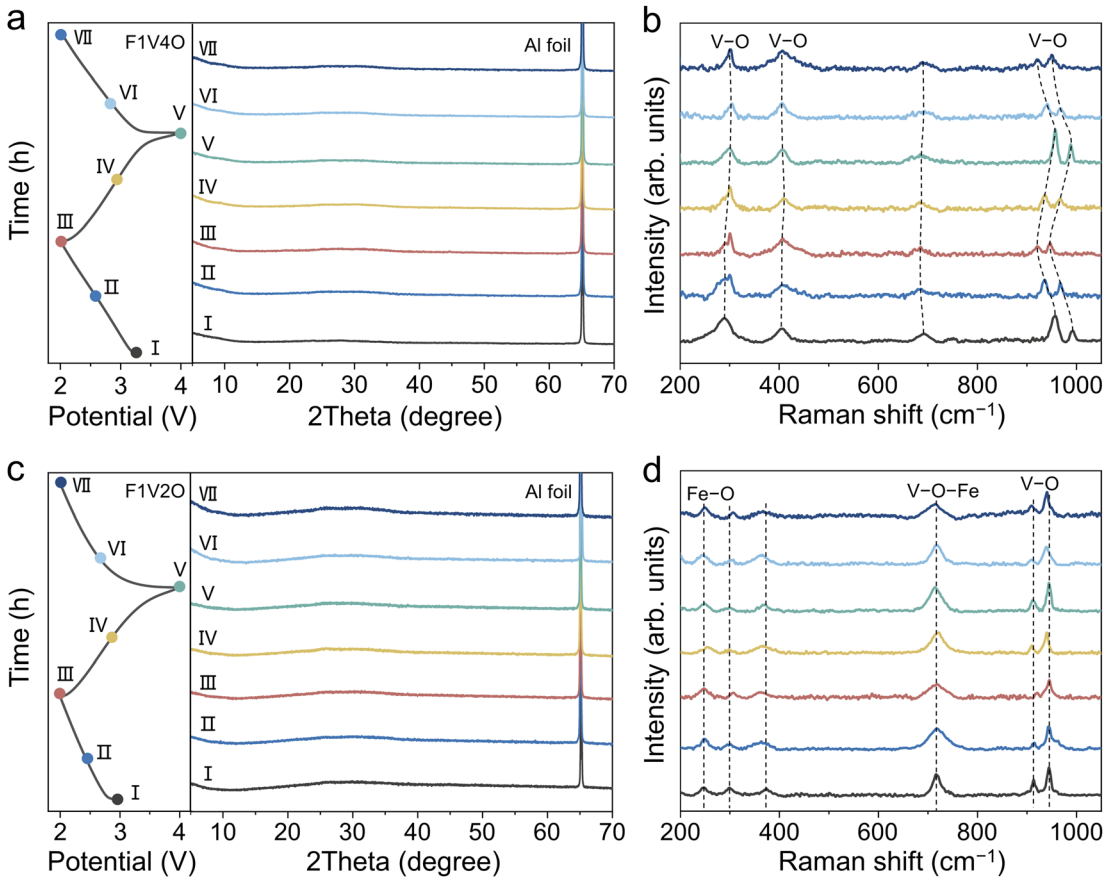

Fig. 5 (a) *Ex situ* XRD patterns and (b) *ex situ* Raman spectra of the F1V4O electrode. (c) *Ex situ* XRD patterns and (d) *ex situ* Raman spectra of the F1V2O electrode.

achieve better kinetics, which is consistent with the experimental results (Fig. 3d).

To analyze the kinetics of the charge storage process, cyclic voltammetry (CV) measurements at varying sweep rates were conducted on the a-FVO electrodes. All three electrodes show quasi-rectangular CV curves with uniformly increasing current intervals as the sweep rate increases (Fig. 4c and S6). A quantitative deconvolution of the charge storage process was performed to separate the current response (i) into capacitive (k_1v) and diffusion-controlled ($k_2v^{1/2}$) contributions using eqn (2).[44]

$$i(v) = k_1 v + k_2 v^{\frac{1}{2}} \quad (2)$$

Fig. S7 shows the capacitive contribution of the current response in the CV curves for the three a-FVO electrodes at 1 mV s^{-1}. F1V1O (94%) and F1V2O (89%) have a higher capacitive contribution than F1V4O (78%) (Fig. 4d and S7), confirming faster charge-transfer kinetics and superior pseudocapacitive behaviors for the former two samples. For F1V4O, the increased diffusion-controlled contribution may originate from the stronger hindrance between V–O bonds with high bond energy and Na^+ ions.[45,46] With the increase in Fe/V ratios, the gradually decreased capacitive contribution indicates that the Fe–O–V bridging bonds significantly modulate the pseudocapacitive response (Fig. 4d).

The Na^+ diffusivity (D_{Na^+}) and kinetic hysteresis during cycling were measured *via* the galvanostatic intermittent titration technique (GITT).[47] The apparent D_{Na^+} with sufficient relaxation time was calculated using eqn (3).

$$D_{Na^+} = \frac{4}{\pi\tau}\left(\frac{mV_m}{MS}\right)^2\left(\frac{\Delta E_s}{\Delta E_t}\right)^2 \quad (3)$$

where τ is the duration of the current pulse, m is the mass of the active material, V_m is the molar volume, S is the active surface area, M is the molar mass, ΔE_s represents the quasi-steady-state potential difference, and ΔE_t refers to the transient potential difference during the current pulse. Fig. 4e displays the relaxation curves of a-FVO electrodes with different Fe/V ratios at 0.02 A g^{-1}. The calculation results show that D_{Na^+} of the F1V2O electrode is 10^{-9}–10^{-10} cm^2 s^{-1} (Fig. 4f), lying between those of F1V1O and F1V4O. The potential difference (E_t–E_s) between the transient potential and quasi-steady state potential also reveals an Fe/V ratio-dependent polarization behavior (Fig. 4f). All three electrodes exhibit a low E_t–E_s value (<0.1 V) with a slight increase during the final stage of desodiation (3.5–4.0 V). Overall, the calculated activation energy, capacitive contribution and Na^+ diffusivity results demonstrate the critical role of the Fe–O–V bonds in determining the electrode reaction kinetics.

2.5 Structural evolution

Ex situ XRD and Raman spectroscopy were carried out to investigate the structural evolution of a-FVO electrodes during electrochemical sodiation and desodiation. XRD patterns of the F1V4O electrode retain its pristine amorphous characteristics throughout the electrochemical pre-sodiation and subsequent cycling (Fig. 5a). In contrast, its *ex situ* Raman spectra reveal slight local structural variations. During initial pre-sodiation to 2.0 V, peaks assigned to the V–O bonds at 690 and 960 cm^{-1} both slightly shift toward lower Raman shifts, accompanied by an increase in the full width at half maximum (FWHM) (Fig. 5b). The increase in FWHM suggests increased structural disorder and heterogeneity in the local bonding environments, which create a more tortuous pathway for Na^+ diffusion, thereby increasing the diffusion-controlled contribution in response currents and slowing down the reaction kinetics. During subsequent desodiation and sodiation processes, the peaks corresponding to V–O bonds return to their pristine positions and then shift again to lower Raman shifts, accompanied by partial narrowing and broadening of their FWHM. The red shifts of the Raman peaks in F1V4O could arise from local bonding expansion or distortion around Fe/V centers after Na^+ insertion, thereby slowing down the rapid transport of Na^+ ions with increasing sodiation depth. This indicates that the local environment of internal V–O bonds may be altered when F1V4O reacts with Na^+ ions, thereby hindering sodium-ion transport.[48] Thus, a lower Fe/V ratio endows F1V4O with abundant active sites to yield high specific capacity, while the enhanced intermolecular interactions restrict charge-transport kinetics. For the F1V2O electrode, *ex situ* XRD patterns show that it retains its pristine amorphous characteristics during initial electrochemical pre-sodiation and subsequent cycling (Fig. 5c), indicating the absence of long-range structural phase transitions. At the local structural level, *ex situ* Raman spectra capture slight changes in the bonding configuration of F1V2O during electrochemical cycling. During the pre-sodiation process, the FWHM and peak positions of the Fe–O bonds at 247, 297 and 372 cm^{-1} remain unchanged (Fig. 5d), while the FWHM of the Fe–O–V bridging bond at 716 cm^{-1} and the V–O bond at 945 cm^{-1} are slightly broadened. This indicates that charge storage reactions preferentially occur at vanadium sites,[40,41] thereby accounting for the higher specific capacity of F1V2O than that of F1V1O (Fig. 3b). Compared with F1V4O, the FWHM of the Fe–O–V and V–O bonds in F1V2O are slightly compressed and broadened during subsequent desodiation and sodiation processes, confirming smaller structural evolution. In the optimal F1V2O composition, the abundant Fe–O–V bridging bonds construct a highly interconnected and flexible local structure. This structure may facilitate rapid Na^+ diffusion through low-energy pathways, thus enabling it to exhibit better performance than F1V1O and F1V4O.

These results indicate that optimizing the Fe/V ratio of a-FVO electrodes enhances the pseudocapacitive response and mitigates structural evolution, thereby achieving excellent cycling stability (Fig. 3f).

3 Conclusions

In summary, we systematically investigated the correlation between the composition (Fe/V ratios) of a-FVO positive electrodes and their electrochemical sodium-ion storage properties. Tuning the Fe/V ratio modulated the valence states of cations and the local bonding configurations, thereby significantly optimizing storage and diffusion abilities for Na^+ ions. Decreasing the Fe/V ratio increased the number of redox-active V sites within the structure, leading to enhanced specific capacity. Kinetic analysis revealed that the electrodes enriched with Fe–O–V bridging bonds exhibited lower charge-transfer activation energy, enhanced capacitive contribution and improved Na^+ diffusivity. Compositional optimization revealed that the F1V2O electrode contained an optimal content of Fe–O–V bridging bonds, achieving a favorable balance between specific capacity (85.5 mAh g^{-1} at 0.05 A g^{-1}) and rate performance (38.2 mAh g^{-1} at 15 A g^{-1}). Based on the kinetic analysis of charge storage, the pseudocapacitive Na^+ storage mechanism of F1V2O was elucidated. During cycling, it retained the pristine amorphous structure without phase transitions, and only involved slight local bond elongation and contraction. This work provides insights into the crucial function of compositional engineering in regulating the reaction kinetics and electrochemical performance of multimetal oxide electrodes, offering guidance for the development of high-capacity and high-rate positive electrodes for future SIHCs.

Author contributions

Xiaoqing Chang: conceptualization, investigation, methodology, writing – original draft. Dafu Tang: investigation, formal analysis, data curation, writing – original draft. Sicheng Fan: formal analysis, data curation. Guiyang Gao: data curation, validation. Qiulong Wei: conceptualization, supervision, project administration, funding acquisition, writing – review and editing. All authors discussed the results and approved the final version of the manuscript.

Conflicts of interest

The authors declare no competing interests.

Data availability

The data supporting this article have been included as part of the supplementary information (SI). Supplementary information: experimental section, XRD data of the samples, SEM micrographs of the electrodes, and electrochemical data. Additional data will be available from the corresponding author upon reasonable request. See DOI: https://doi.org/10.1039/d6ta02103d.

Acknowledgements

This work was supported by the National Natural Science Foundation of China (No. 525B2014, 22479123 and 22179113) and the Fujian Provincial Natural Science Foundation of China (Grant No. 2025J010006).

References

1 C. Zhao, Q. Wang, Z. Yao, J. Wang, B. Sánchez-Lengeling, F. Ding, X. Qi, Y. Lu, X. Bai, B. Li, H. Li, A. Aspuru-Guzik, X. Huang, C. Delmas, M. Wagemaker, L. Chen and Y.-S. Hu, *Science*, 2020, **370**, 708–711.

2 S. Mariyappan, P. Desai, M. Morcrette and J. M. Tarascon, *Nat. Sustain.*, 2026, **9**, 360–371.

3 A. Yao, S. M. Benson and W. C. Chueh, *Nat. Energy*, 2025, **10**, 404–416.

4 A. Rudola, R. Sayers, C. J. Wright and J. Barker, *Nat. Energy*, 2023, **8**, 215–218.

5 P. Cai, K. Zou, X. Deng, B. Wang, M. Zheng, L. Li, H. Hou, G. Zou and X. Ji, *Adv. Energy Mater.*, 2021, **11**, 2003804.

6 X. Gao, H. Wu, C. Su, C. Lu, Y. Dai, S. Zhao, X. Hu, F. Zhao, W. Zhang, I. P. Parkin, C. J. Carmalt and G. He, *Energy Environ. Sci.*, 2023, **16**, 1364–1383.

7 J. Ding, W. Hu, E. Paek and D. Mitlin, *Chem. Rev.*, 2018, **118**, 6457–6498.

8 Z. Xu and J. Wang, *Adv. Energy Mater.*, 2022, **12**, 2201692.

9 Q. Wei, X. Chang, D. Butts, R. DeBlock, K. Lan, J. Li, D. Chao, D.-L. Peng and B. Dunn, *Nat. Commun.*, 2023, **14**, 7.

10 D. Tang, R. Yu, Y. Jiang, J. Li, Z. Yan, S. Fan, X. Huang, S. Lee, T. Li, Q. Xie, L. Mai, D.-L. Peng and Q. Wei, *Nat. Commun.*, 2025, **16**, 2015.

11 Z. Fang, S. Fan, Z. Yan, D. Tang, X. Gao, X. Huang, H. Zheng, B. Wang, Q. Jiang, J. Han, J. Lin, Q. Xie, D.-L. Peng and Q. Wei, *Adv. Mater.*, 2025, **37**, 2412636.

12 J. Pan, Z. Sun, X. Wu, T. Liu, Y. Xing, J. Chen, Z. Xue, D. Tang, X. Dong, H. Zhang, H. Liu, Q. Wei, D.-L. Peng, K. Amine and Q. Zhang, *J. Am. Chem. Soc.*, 2025, **147**, 3047–3061.

13 X. Huang, Y.-f. Cheng, H. Liu, X. Chang, G. Gao, Z. Yan, Q.-q. Wu, Y. Zhong, G. Chen, Z. Peng, D.-L. Peng, J.-h. Chen, G. Zhong and Q. Wei, *ACS Nano*, 2025, **19**, 7168–7177.

14 X. Chang, T. Huang, J. Yu, J. Li, J. Wang and Q. Wei, *Batter. Supercaps*, 2021, **4**, 1567–1587.

15 P. Li, T. Shang, X. Dong, H. Li, Y. Tao and Q.-H. Yang, *Small*, 2021, **17**, 2007548.

16 H. Shao, Y.-C. Wu, Z. Lin, P.-L. Taberna and P. Simon, *Chem. Soc. Rev.*, 2020, **49**, 3005–3039.

17 C. Choi, D. S. Ashby, D. M. Butts, R. H. DeBlock, Q. Wei, J. Lau and B. Dunn, *Nat. Rev. Mater.*, 2020, **5**, 5–19.

18 S. Fleischmann, J. B. Mitchell, R. Wang, C. Zhan, D.-e. Jiang, V. Presser and V. Augustyn, *Chem. Rev.*, 2020, **120**, 6738–6782.

19 T. Guo, P. Hu, L. Li, Z. Wang and L. Guo, *Chem*, 2023, **9**, 1080–1093.

20 H. Ma, B. Zhao, J. Bai, P. Wang, W. Li, Y. Mao, X. Zhu, Z. Sheng, X. Zhu and Y. Sun, *Adv. Sci.*, 2023, **10**, 2203552.

21 L. Han, K. Chen, X. Chen, Y. Zhao, M. Li, C. Liu, Y. Cao and Y. Fang, *Nano Energy*, 2025, **139**, 110986.

22 Q. Wei, Q. Wang, Q. Li, Q. An, Y. Zhao, Z. Peng, Y. Jiang, S. Tan, M. Yan and L. Mai, *Nano Energy*, 2018, **47**, 294–300.

23 Q. Wei, Y. Jiang, X. Qian, L. Zhang, Q. Li, S. Tan, K. Zhao, W. Yang, Q. An, J. Guo and L. Mai, *iScience*, 2018, **6**, 212–221.

24 X.-H. Ma, F. Zhang, Y.-Y. Wei, J.-H. Zhou, J. Wang, W. Jia, Z.-F. Zi and J.-M. Dai, *J. Alloys Compd.*, 2018, **768**, 181–189.

25 D. Xia, H. Gao, M. Li, F. Gong and M. Li, *Energy Storage Mater.*, 2021, **35**, 169–191.

26 Y. Jiang, F. Wu, Z. Ye, C. Li, Y. Zhang, L. Li, M. Xie and R. Chen, *Adv. Funct. Mater.*, 2021, **31**, 2009756.

27 B. Wang, Z. Fang, Q. Jiang, D. Tang, S. Fan, X. Huang, J. Li, D.-L. Peng and Q. Wei, *ACS Nano*, 2024, **18**, 798–808.

28 M. Vincent, S. S. Kumar and D. Kowalski, *Electrochim. Acta*, 2023, **469**, 143161.

29 M. Fiore, G. Longoni, S. Santangelo, F. Pantò, S. Stelitano, P. Frontera, P. Antonucci and R. Ruffo, *Electrochim. Acta*, 2018, **269**, 367–377.

30 A. Š. Vuk, B. Orel, G. Dražič, F. Decker and P. Colomban, *J. Sol–Gel Sci. Technol.*, 2002, **23**, 165–181.

31 Y. Zhao, K. Yao, Q. Cai, Z. Shi, M. Sheng, H. Lin and M. Shao, *CrystEngComm*, 2014, **16**, 270–276.

32 R. Baddour-Hadjean and J.-P. Pereira-Ramos, *Chem. Rev.*, 2010, **110**, 1278–1319.

33 M. C. Biesinger, B. P. Payne, A. P. Grosvenor, L. W. M. Lau, A. R. Gerson and R. S. C. Smart, *Appl. Surf. Sci.*, 2011, **257**, 2717–2730.

34 L. Zhao, T. Wang, F. Li, Y. Liu, F. Zuo, L. Yang, Y. Xu, C. Zhang, H. Wang, J. Liu, X. Dong, S. Zhu, Q. Li and H. Li, *Chem. Eng. J.*, 2023, **452**, 139310.

35 T. Huang, J. Yu, X. Huang, J. Li, B. Wang, Y. He, D. Tang, J. Zhang, D.-L. Peng, K. Lan and Q. Wei, *Small Struct.*, 2023, **4**, 2300165.

36 K. O. Adeniyi, B. Osmanaj, G. Manavalan, A. Samikannu, J.-P. Mikkola, B. Avni, J.-F. Boily and S. Tesfalidet, *Electrochim. Acta*, 2023, **458**, 142538.

37 A. P. Grosvenor, B. A. Kobe, M. C. Biesinger and N. S. McIntyre, *Surf. Interface Anal.*, 2004, **36**, 1564–1574.

38 H. Niu, H. Liu, W.-H. Huang, T. Shen, M. Yang, M.-H. Yeh, L. Yang and C. Liu, *Adv. Funct. Mater.*, 2026, **36**, e18785.

39 H. Liu, H. Niu, W.-H. Huang, T. Shen, C. Li, C.-C. Chang, M. Yang, C. Gao, L. Yang, Q. Zong, Y. Pei, G. Cao and C. Liu, *ACS Energy Lett.*, 2024, **9**, 5492–5501.

40 M. Chen, Q. Liu, Z. Hu, Y. Zhang, G. Xing, Y. Tang and S.-L. Chou, *Adv. Energy Mater.*, 2020, **10**, 2002244.

41 T. Liu, Y. Liu, C. Niu and Z. Chao, *ChemElectroChem*, 2022, **9**, e202101493.

42 K. Li, J. Zhang, D. Lin, D.-W. Wang, B. Li, W. Lv, S. Sun, Y.-B. He, F. Kang, Q.-H. Yang, L. Zhou and T.-Y. Zhang, *Nat. Commun.*, 2019, **10**, 725.

43 J. Sun, L. A. O'Dell, M. Armand, P. C. Howlett and M. Forsyth, *ACS Energy Lett.*, 2021, **6**, 2481–2490.

44 Q. Wei, X. Chang, D. Butts, R. DeBlock, K. Lan, J. Li, D. Chao, D.-L. Peng and B. Dunn, *Nat. Commun.*, 2023, **14**, 7.

45 Q. Miao, M. Li and B. Yan, *Metals*, 2023, **13**, 1498.

46 W. Xie, X. Xing and Z. Cao, *J. Am. Ceram. Soc.*, 2020, **103**, 3797–3811.

47 Y.-C. Chien, H. Liu, A. S. Menon, W. R. Brant, D. Brandell and M. J. Lacey, *Nat. Commun.*, 2023, **14**, 2289.

48 X. Zhang, Z. Zhang, S. Xu, C. Xu and X. Rui, *Adv. Funct. Mater.*, 2023, **33**, 2306055.